Photoelectron imaging spectrometry: Principle and inversion method

C. Bordas and F. Paulig
Laboratoire de Spectrométrie Ionique et Moléculaire, Université Claude-Bernard Lyon I, 43 Boulevard du 11 Novembre 1918, F69622 Villeurbanne, France

H. Helm
Fakultät für Physik, Universität Freiburg, Hermann-Herder-Strasse 3, D79104 Freiburg, Germany

D. L. Huestis
Molecular Physics Laboratory, SRI International, Menlo Park, California 94205

(Received 24 January 1996; accepted for publication 28 February 1996)

A new photoelectron spectrometer has recently been used to analyze the energy and spatial distribution of photoelectrons produced by multiphoton ionization of rare gases. It is based on the analysis of the image obtained by projecting the expanding electron cloud resulting from the ionization process onto a two-dimensional position sensitive detector by means of a static electric field. In this article, we present the principle of this imaging spectrometer and the relevant equations of motion of the charged particle in this device, together with an inversion method that allows us to obtain the energy and angular distribution of the electrons. We present here the inversion procedure relevant to the case where the electrostatic energy acquired in the static field is large as compared to the initial kinetic energy of the charged particles. A more general procedure relevant to any regime will be described in a following article. © *1996 American Institute of Physics.* [S0034-6748(96)02706-2]

I. INTRODUCTION

Photoelectron spectroscopy[1] has been widely used in the past decades to study photoionization or photodetachment processes of various species from atoms[2–5] to clusters,[6–8] including small or complex molecules.[9–13] Most of the techniques applied so far are based on energy resolution by time of flight (TOF) measurements or employ electrostatic analyzers for energy analysis. These spectrometers[10,13] allow one to measure both energy and angular distributions. However, the energy distribution is obtained for only a single orientation of the laser polarization at one time, and both energy and angular resolution are good to the extent that the acceptance angle of the spectrometer is small. As a consequence, the detection efficiency of this kind of photoelectron spectrometer is low, on the order of 10^{-5} to 10^{-4}. In order to improve the detection efficiency without loss of resolution, an inhomogeneous magnetic field may be combined with the TOF principle. This is done in the so-called magnetic bottle spectrometer.[14] In this spectrometer, all electrons emitted in a solid angle of 2Π or 4Π sr, according to the design of the apparatus, are detected. However, the measurement of the angular distribution, although possible, is not compatible with the detection of all electrons simultaneously and is usually not attempted in practice. Standard TOF spectrometers, electrostatic analyzers, and magnetic bottles give an energy resolution in the range of 10–100 meV but suffer a substantial decrease in the detection efficiency at low energy. Simultaneously, the relative energy resolution is poor near threshold. The zero electron kinetic energy photoelectron spectrometer (ZEKE–PES)[15–17] is specially tailored to handle this kind of phenomenology: namely, the study of threshold electrons. However, this technique has several limitations inherent to its principle. The ZEKE-PES has a very restricted range of energy (a fraction of meV above threshold) and moreover it does not provide angular information. Hence, there is a real need for a new kind of photoelectron spectrometer combining high detection efficiency, including low velocity electrons, reasonable resolution, and simultaneous measurements of angular distributions. The imaging spectrometer introduced in 1993[18] combines the advantages of the different methods mentioned above by making use of the possibilities offered by recent two-dimensional detection techniques. In this article we describe the principle of this technique and focus our attention on the inversion method required to extract the physical information from electron images in the simple case corresponding to current experimental setups. The general method, applicable to any regime of the imaging spectrometer, poses essentially different algebraic problems that will be discussed in a separate article.

II. PRINCIPLE OF THE SPECTROMETER

A. Principle

The principle of the photoelectron imaging spectrometer is based on a very simple idea: photoelectrons produced at time $t=0$ at a point source ($r=0$) with a given kinetic energy W_0 are found later on the surface of a sphere of radius r_t expanding with time according to:

$$r_t = \sqrt{\frac{2W_0}{m}}\, t. \tag{1}$$

For instance, electrons emitted with an initial kinetic energy of 1 eV are found after 20 ns on the surface of a sphere of radius 12 mm. If we then apply ''instantaneously'' a high electrostatic field, this sphere can be projected onto a position sensitive detector, producing an image that contains all the spatial and energy information relevant to the process. In

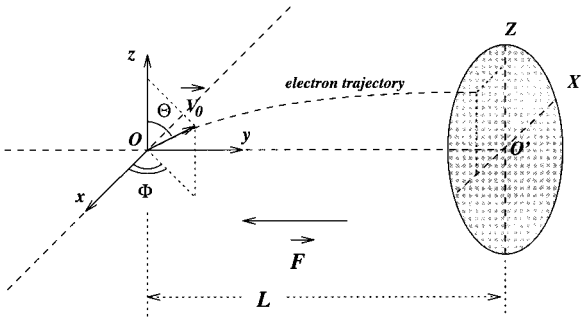

FIG. 1. Schematic of the projection method. Photoelectrons generated at a point source O are accelerated towards a plane position sensitive detector by means of a homogeneous electric field.

fact, this principle must be slightly modified in order to avoid the problems related to the definition of an infinite electric field established at a given time $t=0$. A more realistic experiment, although analogous under certain conditions, consists of producing the photoelectrons in a region where a homogeneous and constant electric field is applied. The static field is used to project the electrons onto the detector. We will see that, provided that the electrostatic energy gained in the field is by far larger than the initial kinetic energy, one obtains the same image as in the hypothetical experiment described above. This experimental principle is shown schematically in Fig. 1.

B. Derivation of the equations of motion

Let O be the point at which the electrons are emitted, defined by its coordinates $x_0=y_0=z_0=O$, and O' the center of the position sensitive detector $x_{0'}=z_{0'}=O$ and $y_{0'}=L$, the distance between the region of interaction where photoelectrons are emitted and the detector. A homogeneous electric field is applied along the Oy axis. We propose that the photoionization, or photodetachment, process is induced by light polarized along the Oz axis, parallel to the plane detector according to Fig. 1. If an electron is ejected at O with an initial kinetic energy W_0 along the direction (Θ,Φ), the components of its initial velocity $\mathbf{v}_0$ are defined by

$$\begin{aligned} v_{0x}&=v_0 \sin\Theta \cos\Phi,\\ v_{0y}&=v_0 \sin\Theta \sin\Phi,\\ v_{0z}&=v_0 \cos\Theta, \end{aligned} \tag{2}$$

with $W_0=\frac{1}{2}mv_0^2$, where m is the electron mass.

The homogeneous electric field $\mathbf{F}$, parallel to the Oy axis and perpendicular to the detector, projects this electron onto the detector surface. The coordinates of the impact on the detector can be derived using very simple algebra. Using the coordinate axis defined in Fig. 1, one finds that these coordinates are

$$\begin{aligned} X&=\frac{2L \cos\Phi \sin\Theta}{\rho}\\ &\quad\times(\sqrt{\sin^2\Phi \sin^2\Theta+\rho}-\sin\Phi \sin\Theta),\\ Z&=\frac{2L \cos\Theta}{\rho}(\sqrt{\sin^2\Phi \sin^2\Theta+\rho}-\sin\Phi \sin\Theta), \end{aligned} \tag{3}$$

where

$$\rho=\frac{qFL}{W_0} \tag{4}$$

is the ratio between the electrostatic energy acquired in the field and the initial kinetic energy of the electron (q is the elementary charge).

Electric dipole selection rules and a linear polarization of the laser field along Oz lead to an initial angular distribution that is cylindrically symmetric around Oz, i.e., it is independent on the angle Φ but depends only on the angle Θ and on the energy W_0. Hence, we can assign a given angular distribution $F(W_0,\Theta)$ at each energy channel that represents the number of electrons emitted in the solid angle Ω defined by (Θ,Φ). One immediately sees that, in order to preserve the information relative to this distribution in the image obtained on the detector, the laser polarization must be parallel to the detector. On the contrary, if the laser polarization was set perpendicular to the detector, the image would be symmetric around this axis, i.e., around point O'. Under such conditions, extracting both angular and energy distribution from the image would not be possible.

The first step in understanding the experimental process is to pay attention to the geometry of the impact positions as a function of the initial conditions. For this purpose, it is convenient to work with the dimensionless units ρ, X/L, and Z/L. This is done in Fig. 2, where we have plotted the relative coordinates of impact $(X/L,Z/L)$ for different values of ρ, and for Θ varying between 0° and 180° by steps of 10°, and for all possible values of Φ. The simplest case is obtained when ρ is large compared to unity. Indeed, when ρ tends to infinity, Eqs. (3) reduce to:

$$\begin{aligned} X&=\frac{2L \cos\Phi \sin\Theta}{\sqrt{\rho}},\\ Z&=\frac{2L \cos\Theta}{\sqrt{\rho}}. \end{aligned} \tag{5}$$

That is to say, for a given energy (i.e., a given ρ), electrons emitted along an initial direction Θ are found on the detector along a straight line of constant Z with $|X|\leqslant 2L \sin\Theta/\sqrt{\rho}$. This is clearly seen in Fig. 2(a), where $\rho=10^4$. This simple arrangement is no longer observed when the ratio ρ decreases. For example, at $\rho=100$ [see Fig. 2(b)], the electrons ejected with a given Θ are found on a quasielliptical contour, the electrons traveling initially towards the detector being found closer to O' than those traveling outwards. When one decreases ρ further, the situation is even more complicated and one reaches the patterns of Figs. 2(c) and 2(d) (respectively, $\rho=1$ and 10^{-6}), where the link between impact position and original conditions is far from being simple. In the limit $\rho\to 0$ [see Fig. 2(d)], one can see complex patterns for different values of Θ. Under such conditions (initial kinetic energy much larger than electrostatic energy), the electrons emitted towards the detector fall on its center O', while those emitted in the opposite direction are ejected far away from O'. From these considerations, we can deduce easily that extracting the original distribution $F(W_0,\Theta)$ from the ex-

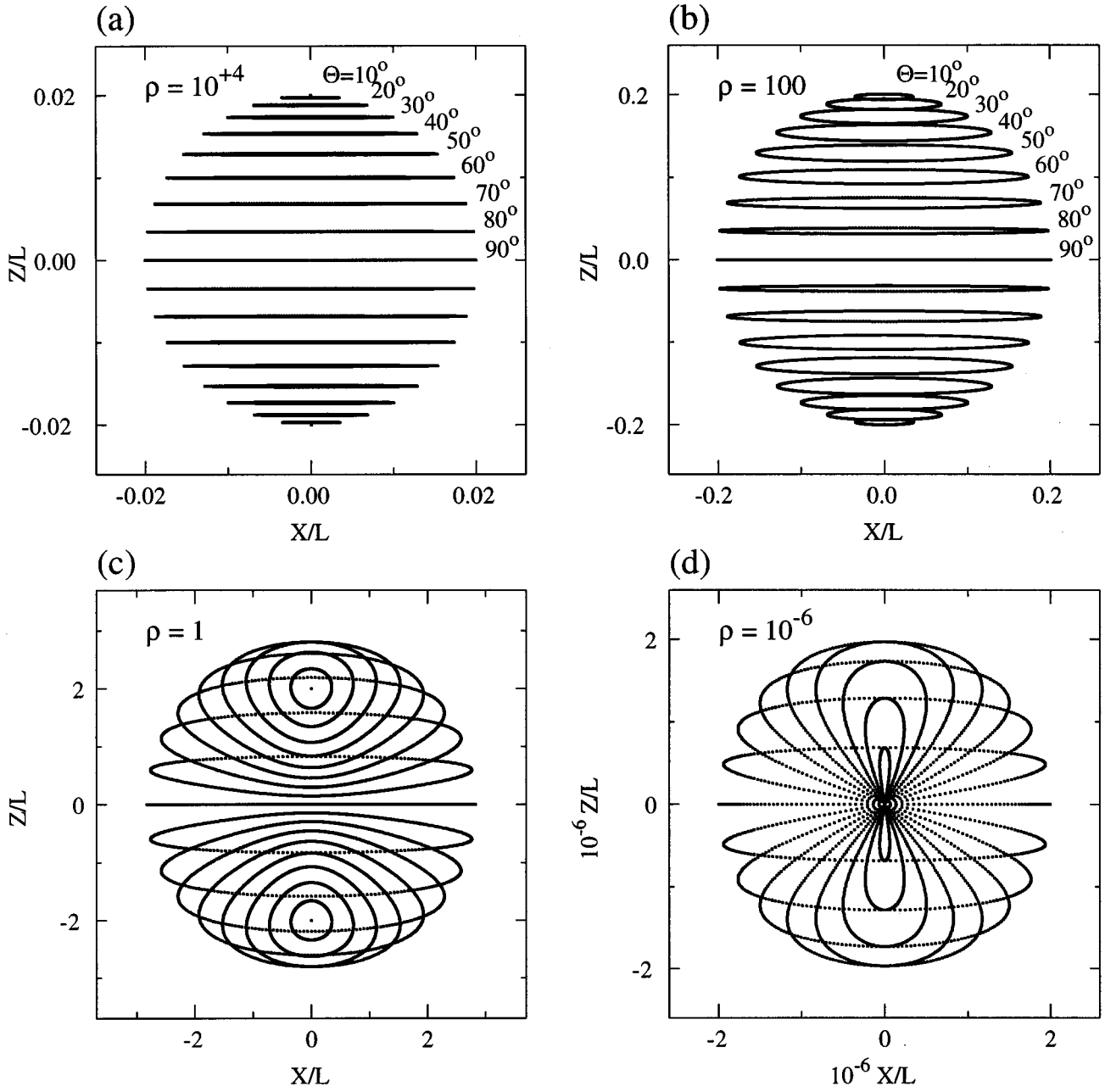

FIG. 2. Projection pattern for various values of ρ in the dimensionless units: ρ, X/L, and Z/L. The relative coordinates of impact $(X/L, Z/L)$ are plotted for different values of ρ, and for Θ varying between 0° and 180° by steps of 10°, and for all possible values of Φ. (a) $\rho=10^4$; in that case, electrons emitted along an initial direction Θ are found on the detector along a straight line of constant Z. (b) $\rho=100$; the electrons ejected with given Θ are found on a quasielliptical contour, the electrons traveling initially towards the detector being found closer to $0'$ than those traveling outwards. (c) $\rho=1$. (d) $\rho=10^{-6}$; complex patterns for different values of Θ. Under such conditions $(W_0 \gg qFL)$, the electrons emitted towards the detector fall close to its center $0'$ while those emitted in the opposite direction are ejected far away from $0'$.

perimental data is, in general, a complex two-dimensional operation for arbitrary values of ρ. Fortunately, owing to Eq. (5), this operation reduces to a much simpler one-dimensional transformation in the limit $\rho \to \infty$. Hence, in the following, we will discuss the processing of the image in this limit.

Prior to this discussion, let us derive some simple quantities from the exact equations of motion [Eqs. (3)]. Let us first invert these equations. One finds that for a given value of the ratio ρ, two different initial directions of ejection lead the electron to a given (X,Z) position on the detector, namely, the set of angles (Θ^+,Φ^+) and (Θ^-,Φ^-) defined by

$$\Phi^{\pm} = \arctan\left(\frac{-2 \pm \sqrt{4(\rho+1) - [\rho^2(X^2+Z^2)/L^2]}}{\rho X/L} \right),$$
$$\Theta^{\pm} = \arctan\left(\frac{X}{Z \cos \Phi^{\pm}} \right). \tag{6}$$

These equations have two important consequences. The first one is that two different original trajectories corresponding to the same initial kinetic energy can lead to the same impact

position. This leads to interference patterns that could be in principle observed on the detector. For presently realizable systems, this pattern cannot be resolved and we will not discuss this point further in this article. The second consequence is more trivial: Eqs. (6) are defined only for accessible (X,Z) couples, i.e., Eqs. (6) determine simply the maximum radius of the image, in other words, the maximum distance from O' to the impact position. Indeed, this radius $R=\sqrt{X^2+Z^2}$ must be smaller than $R_{\max}$ in order to get a positive argument under the square root in Eq. (6) with:

$$R_{\max}=2L\,\frac{\sqrt{\rho+1}}{\rho}. \tag{7}$$

This means that, when defining an experimental geometry, in particular the effective radius R_0 of the position sensitive detector and the distance L between the ionization region and the detector, one automatically imposes the lowest ρ value corresponding to the largest image visible in the system:

$$\rho_{\min}=\frac{1+\sqrt{1+(R_0^2/L^2)}}{R_0^2/2L^2}, \tag{8a}$$

which reduces to

$$\rho_{\min}=\left(\frac{2L}{R_0}\right)^2 \tag{8b}$$

for large ρ values.

The smallest value of ρ is thus entirely defined by the experimental geometry. Therefore, the spectrometer may be designed in order to operate only at large ρ values where a one-dimensional transformation is sufficient: for example, imposing $\rho\geqslant 1000$ is equivalent to set $L\geqslant 16R_0$. However, this does not mean that the exact 2D transformation is irrelevant simply because one can imagine particular experimental problems, or a specific environment, where the ionization region must be close to the detector as compared to its dimension. Under such conditions, $L\ll R_0$ and ρ is small. This is the case, for instance, if one wishes to work with a very low electric field, which can be required for studying very excited states. The exact 2D inversion procedure relevant to any value of ρ is essentially different from a technical point of view and raises specific analytical and numerical problems that will be discussed separately. This exact transformation may in particular allow to built very compact imaging spectrometer with an extremely short L distance that can fit in any environment.

C. Experimental setup

A schematic view of our experimental setup is shown in Fig. 3. A homogeneous electric field (typically 10 to 200 V/cm) is established by a set of cylindrical guard rings. The region of homogeneous field is about 10 cm long and 7 cm wide. On the high potential side, this region ends up with the 2D detector itself. Helmoltz coils mounted outside the vacuum chamber or μ-metal screen are used to reduce the earth's and parasite magnetic fields. For a typical experiment on multiphoton ionization of gases, the vacuum chamber is filled with 10^{-5} Torr of the gas of interest (xenon, hydrogen, ...). The laser beam is focused by a 15 cm lens to the center

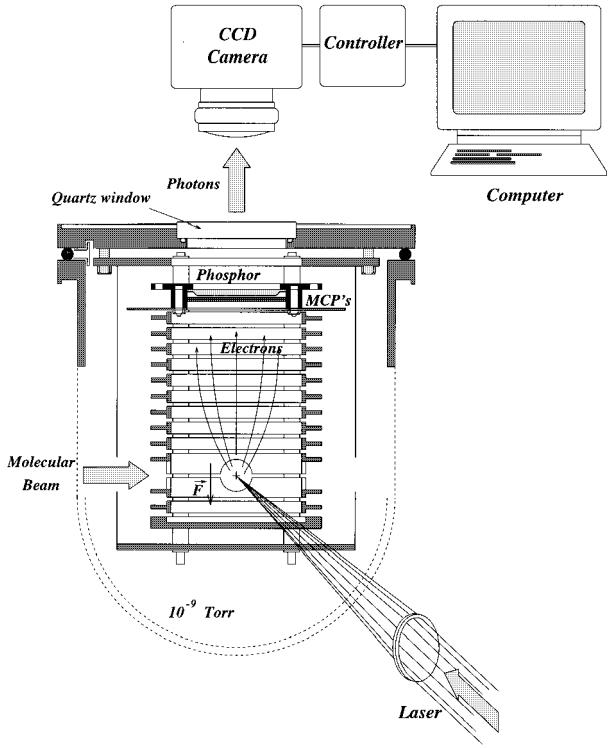

FIG. 3. Schematic of the photoelectron imaging spectrometer.

of the acceleration region. Under these conditions, the volume of the electron source, where multiphoton ionization occurs, is about 100 μm^3. The detector is made of a tandem microchannel plate of 2 in. diameter positioned at one end of the spectrometer. In the case of $\rho\gg 1$, electrons hitting the detector all have about the same kinetic energy, independent of the initial kinetic energy. Hence, the gain, and by way of consequence the detection efficiency, is independent of the initial kinetic energy. Electrons exiting the channel plates are then accelerated to 4–6 kV to impact on an ultrahigh vacuum grade phosphor screen. The screen phosphorescence is accumulated on the charge-coupled-device (CCD) elements of a Tektronix digital camera of 512×512 pixel resolution, and cooled down to about -30°C by a Peltier element. The signal is accumulated in the CCD over a few tens of laser shots before being transferred to a microcomputer via a Princeton Instruments controller. The signal can be summed and averaged over an arbitrary number of laser shots. The diameter of the detector combined with the resolution of the CCD allows us to achieve a geometric resolution of about 100 μm, which is on the same order as the best we can do with the ionization region dimensions. In multiphoton ionization experiments of xenon presented below, one can obtain a significant, although noisy, image with a single laser shot, i.e., about 1000 electrons are detected simultaneously. However, it is recommended to work at low flux in order to avoid space charge effects and saturation of the detector. Notice that, at a pressure of 10^{-5} Torr, about 10^5 atoms lie in the focal volume of the laser. In order to operate properly, the principle of our spectrometer imposes that the dimensions of the ionization region are as small as possible. Indeed, the energy resolution is directly limited by the geometric resolution on the detec-

tor, which is itself limited by the initial dimension of the electron cloud. This is easily achieved in multiphoton ionization experiments where electrons are extracted only in the focal volume of the laser beam, but this poses some practical problems when single photon ionization or detachment are concerned. This is in fact the most limiting restriction to the capabilities of this kind of spectrometer. In single photon experiments, the ionization volume must be defined by the crossing between the laser and the molecular beams instead of being determined only by the laser.

III. IMAGE PROCESSING IN THE LIMIT OF LARGE ENERGY RATIO

The purpose of this section is to describe the numerical procedures used to extract the relevant physical data from raw experimental images, namely, the energy spectrum and the angular distributions. First we will discuss the projection process: giving a certain energy and angular distribution, what is the image obtained on the position sensitive detector and what is the influence of ρ? Second, in the limit $\rho\rightarrow\infty$, how can we invert this image to get back to the original distribution? Owing to the one-dimensional nature of the problem when $\rho\rightarrow\infty$, the usual answer to that kind of problem would be to use a standard Abel inversion.[19] However, instead of using this approximate general method, it is more convenient to use the ''exact'' back-projection method, which can then be extended to the complex 2D transformation relevant to an arbitrary value of ρ. This back projection is exact only in the limit of continuous distribution. Of course, the experimental data are, by nature, discrete, and the finite dimensions of each pixel of the detector introduce some approximations in the transformation. We will discuss this point further.

We will first compare projection and back projection of simulated electronic distributions before presenting some experimental results obtained in four-photon ionization of xenon and molecular hydrogen.

A. Projection

For a given original angular distribution $F(W_0,\Theta)$, two different numerical methods may be used to simulate the projection achieved in the spectrometer. The first one relies on the explicit calculation of the exact Jacobian of the transformation from coordinates (Θ,Φ) to (X,Z) for a given value of ρ. The second one consists in launching a large number of random trajectories statistically distributed according to the original distribution $F(W_0,\Theta)$. In this article, the first method will be used only in the limit $\rho\rightarrow\infty$, while the second method will be used for finite values of ρ. This distinction is made simply to avoid the complexity of the general transformation and of the associated singularities that will be discussed elsewhere. Electrons emitted in a given direction (Θ,Φ) for a given value of ρ will be found on the detector at the position (X,Z) according to Eq. (3). The angular distribution $F(W_0,\Theta)$ or equivalently $F(\rho,\Theta)$ is, by definition, proportional to the number of electrons ejected in the solid angle Ω defined by the Euler angles (Θ,Φ). The corresponding number of electrons hitting the detector at position (X,Z) by unit surface is simply the density $F_d(\rho,X,Z)$, which is related to the original distribution by

$$F_d(\rho,X,Z)S_{XZ}=F(\rho,\Theta)S_{\Theta\Phi}, \tag{9}$$

where $S_{\Theta\Phi}$ and S_{XZ} are, respectively, the elementary surface on the sphere in the initial coordinates and the corresponding surface on the plane detector.

The elementary surface $S_{XZ}=|\mathbf{J}|d\Theta d\Phi$ corresponds to the elementary surface on a sphere of radius L in the initial coordinates $S_{\Theta\Phi}=L^2\sin\Theta\ d\Theta\ d\Phi$, and finally:

$$F_d(\rho,X,Z)=L^2\ \sin\Theta\ |\mathbf{J}|^{-1}F(\rho,\Theta), \tag{10}$$

where the Jacobian $\mathbf{J}$ of the transformation is defined as:

$$\mathbf{J}=\frac{\partial X}{\partial\Theta}\frac{\partial Z}{\partial\Phi}-\frac{\partial X}{\partial\Phi}\frac{\partial Z}{\partial\Theta}. \tag{11}$$

Note that $\sin\Theta$ is always positive since $0\leqslant\Theta\leqslant\Pi$. The general expression of the Jacobian operator $\mathbf{J}$ calculated according to Eqs. (3) and (11) is rather complex; however, it reduces to a fairly simple analytic expression when $\rho\rightarrow\infty$. In that case, the transformation $(X,Z)\leftrightarrow(\Theta,\Phi)$ is given by Eqs. (5) and the expression of the Jacobian reduces to:

$$|\mathbf{J}|=\frac{4L^2}{\rho}\sin^2\Theta|\sin\Phi|, \tag{12}$$

and, accordingly:

$$F_d(\rho,X,Z)=F(\rho,\Theta)\left|\frac{\rho}{4\sin\Theta\ \sin\Phi}\right|. \tag{13}$$

A brief inspection of the set of Eq. (5) shows that for a given ρ, in the limit of large ρ values, the coordinate Z depends only on the angle Θ, while for that given pair of ρ and Z values, X depends only on Φ. Thus, for a given pair of ρ and Z_0 values, one can define the quantity X_0 as the maximum value of X electrons can reach according to Eq. (7) in the limit of large ρ values:

$$R_{\max}=\sqrt{X_0^2+Z_0^2}=\frac{2L}{\sqrt{\rho}},\quad \text{i.e.,}\quad \rho=\frac{4L^2}{X_0^2+Z_0^2}. \tag{14}$$

Equation (5) can be easily inverted as:

$$\begin{aligned}\Theta&=\arccos\left(\frac{\sqrt{\rho}Z_0}{2L}\right),\\ \Phi&=\arccos\left(\frac{X}{X_0}\right).\end{aligned} \tag{15}$$

These equations finally allow us to write down explicitly the relation between the density of electrons of a given initial kinetic energy W_0 (or alternatively ρ) reaching the detector at a given position (X,Z), $F_d(\rho,X,Z)$ and the initial distribution $F(\rho,\Theta)$:

$$F_d(\rho,X,Z)=F(\rho,\Theta)\frac{\rho}{4\sin\Theta\sqrt{1-(X/X_0)^2}}, \tag{16}$$

if $X\leqslant X_0$, and $F_d(\rho,X,Z)=0$ otherwise. This function diverges at $X=X_0$, defined by Eq. (14). The same problem of divergence occurs for finite values of ρ, with the additional problem that the general form of Eq. (16) is by far more

complex. However, the experimental observable is not exactly $F_d(\rho,X,Z)$ but rather its integral over a finite domain defined by the CCD pixel. The integral of $F_d(\rho,X,Z)$ over a finite surface is finite as shown below. All the equations presented above, limited to a single energy channel ρ, can be generalized easily by summing (or integrating) over a given domain of ρ, provided that the ρ values of interest are large enough. As long as one works with continuous variables (X,Z), Eq. (16) holds and the projection method (and correspondingly the inversion method) is exact. Once we take into account the discrete nature of the detector, some approximations must be made. Let us now define the pixel (i,j) of the CCD as the surface defined by $(i-1)d \leqslant X \leqslant id$ and $(j-1)d \leqslant Z \leqslant jd$, where d is the effective size of a (square) pixel. The physical quantity measured in the experiment (for a given ρ) is the number of electrons collected at the pixel position (i,j):

$$\mathscr{I}(i_0,i,j)=\int_{(j-1)\cdot d}^{j\cdot d} dZ \int_{(i-1)\cdot d}^{i\cdot d} F_d(\rho,X,Z)\,dX, \tag{17}$$

where i_0 [with $X_0=(i_0-0.5)d$ defined in Eq. (14)] is the maximum pixel value reachable for a given (ρ,Θ) set. By substituting Eq. (16) in Eq. (17), one finds:

$$\begin{aligned}\mathscr{I}(i_0,i,j)&=\frac{\rho}{4}\int_{(j-1)\cdot d}^{j\cdot d}\frac{F(\rho,\Theta)}{\sin\Theta}\,dZ\int_{(i-1)d}^{id}\frac{dX}{\sqrt{1-(X/X_0)^2}}\\&=\frac{\rho}{4}\int_{(j-1)\cdot d}^{j\cdot d}\frac{F(\rho,\Theta)}{\sin\Theta}\,dZ\left[\arcsin\left(\frac{X}{X_0}\right)\right]_{(i-1)d}^{i\cdot d}X_0,\end{aligned} \tag{18}$$

where Θ and X_0 are functions of the variable Z according to Eqs. (14) and (15). The integration over the variable Z remaining in Eq. (18) is in the following approximated by a simple arithmetic averaging, which consists in substituting Z by its average value over the domain of integration: $Z=(j-0.5)d$. This approximation is supported by the fact that the variation of **J** along the Z axis is very smooth except in the vicinity of the center of the image, which usually contains poor information. This simplification introduced very minor discrepancies for $\Theta=0°$; however, an exact integration of Eq. (18) is not necessary and we can simplify this expression to:

$$\mathscr{I}(i_0,i,j)=\mathscr{F}(i_0,i,j)F(\rho,\Theta_0), \tag{19}$$

with the projection operator defined as:

$$\begin{aligned}\mathscr{F}(i_0,i,j)&=\frac{\rho}{4}\frac{d}{\sin\Theta_0}\left[\arcsin\left(\frac{X}{X_0}\right)\right]_{(i-1)d}^{i\cdot d}X_0,\\&\qquad\text{for } i<i_0,\\\mathscr{F}(i_0,i_0,j)&=\frac{\rho}{4}\frac{d}{\sin\Theta_0}\left(\frac{\Pi}{2}-\arcsin\frac{(i_0-1)d}{X_0}\right)X_0,\end{aligned} \tag{19'}$$

and

$$\mathscr{F}(i_0,i,j)=0 \quad \text{for } i>i_0,$$

with $Z_0=(j-0.5)d$, $X_0=(i_0-0.5)d$, and $\Theta_0=\arctan(X_0/Z_0)$.

Since we are dealing with discrete data, one has to define precisely the coordinates that we use, not only on the detector (which is imposed by experimental conditions), but also in the space of angular and energy coordinates. The most convenient procedure is to define a discrete grid where the radius R is proportional to the initial velocity of the electron, and the angle is the emission angle Θ. The distribution $F(\rho,\Theta)$ is replaced by the function $F_{R\Theta}(i,j)$ defined on a discrete grid with the relation (pixel center: $x_i=i-0.5$; $z_j=j-0.5$):

$$\begin{aligned}&F_{R\Theta}(i,j)=F(\rho,\Theta),\\&\Theta=\arctan(x_i/z_j),\\&\rho=\frac{\rho_0}{(x_i^2+z_j^2)}=\frac{\rho_0}{R_{ij}^2},\end{aligned} \tag{20}$$

where ρ_0 is determined by experimental parameters. This framework presents the advantage that a pixel to pixel correspondence is obtained for the electrons emitted at $R_{\max}$ ($\Phi=0°$ in the present case) between both representations. The final expression for the discrete projection is

for all (i_0,j_0):

$$F_{XZ}(i_0,j_0)=\sum_{i\geqslant i_0}[\mathscr{F}(i,i_0,j_0)F_{R\Theta}(i,j_0)], \tag{21}$$

where F_{XZ} and $F_{R\Theta}$ are the photoelectron distribution as a function of the pixel number in the detector and in the initial coordinates, respectively, and with the projection operator $\mathscr{F}$ defined by Eqs. (19′).

Taking into account the symmetry of the image about the O_X and O_Z axes allows a complete treatment of the distribution. The major difference between Eq. (21) and the general expression (arbitrary ρ) is that the sum reduces to a single variable over the index i (X coordinate), while in the general transformation the sum would run on both indices i and j. Thus, the two-dimensional inversion procedure is reduced to a one-dimensional procedure. Equations (12)–(21) are relevant only under the condition that ρ is large enough. In order to estimate the error introduced by this assumption, we calculate the projection pattern for arbitrary ρ values. In order to avoid the singularities and the complexity of the general expression of the Jacobian, we simulate this case here by launching a large number of electron trajectories distributed according to the initial energy and angular distribution.

Figure 4 illustrates the projection process in a very simple case. The top image of Fig. 4 represents the original electron distribution in the frame (R,Θ) as defined above. The initial velocity distribution is a gaussian profile centered at $R_0=150$ (pixel units) and 10 pixels wide (R is proportional to the initial velocity). $F_{R\Theta}(i,j)$ is plotted in the top figure: the angular distribution is chosen spherically symmetric in this case (Y_{00}^2), i.e., the number of electrons emitted by unit of solid angle is a constant. As a consequence, Fig. 4(a) does not represent the total number of electrons: the actual number of electrons emitted in a given angular region $(\Theta,\Theta+d\Theta)$ is proportional to $[\sin\Theta\, F_{R\Theta}(i,j)d\Theta]$. After projection onto the plane detector, one obtains the image of Fig.

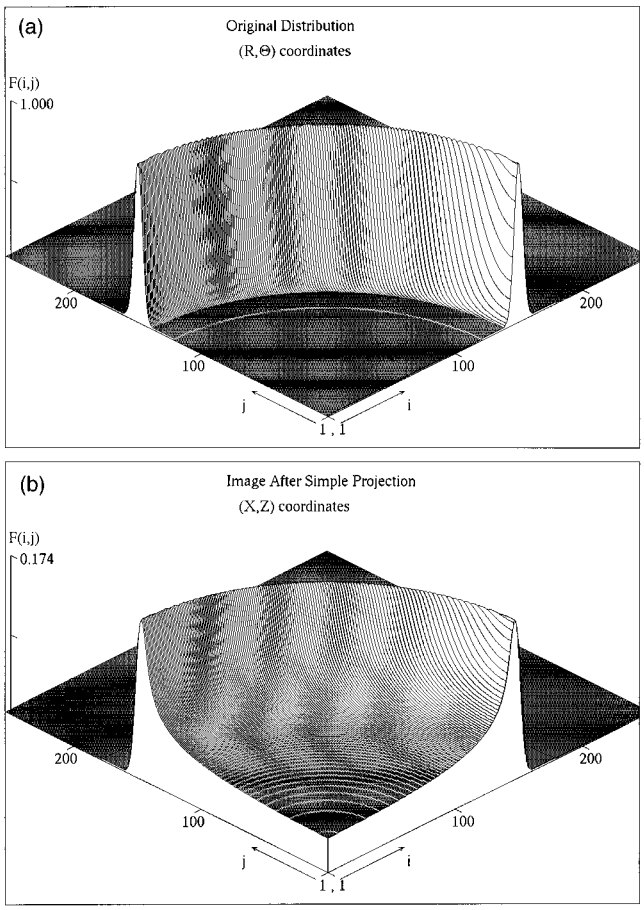

FIG. 4. Projection in a very simple case. The top image (a) represents the original electron distribution in the frame (R,Θ). The initial velocity distribution is a Gaussian profile centered at $R_0=150$ (pixel units) and 10 pixels wide. The angular distribution is chosen spherically symmetric (Y_{00}^2). After projection in the approximation $\rho\rightarrow\infty$, one obtains the bottom image (b), where i and j are the actual position (in pixels, relative to the center of the image) in the detector plane. In this figure and in the following, only one fourth of the image is represented since the angular distribution is symmetric around the laser polarization axis.

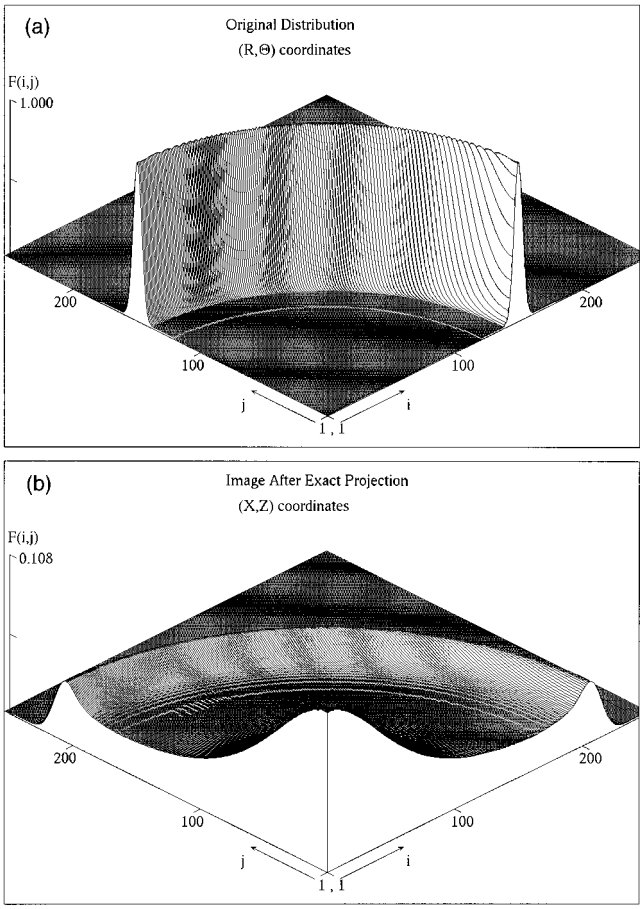

FIG. 5. Same original distribution (a) as in Fig. 4 except that the ratio ρ corresponding to the maximum of the photoelectron distribution is $\rho=1$. The projected image (b) is completely distorted as compared to Fig. 4(b). One can see in particular a broad peak at the center of the image, corresponding to electrons emitted towards the detector, and a larger ring outside corresponding to electrons emitted in the opposite direction.

4(b) (bottom), where i and j are the actual position in the detector plane. In both representations, only one fourth of the image is represented since the angular distribution is symmetric around the laser polarization axis. The effect of the projection is better understood in that representation: the photoelectrons are found mostly at the periphery of the image and smoothly distributed inside. The cylindrically symmetric image of Fig. 4(b) is the ideal pattern expected for electrons emitted isotropically with a Gaussian velocity distribution. Anisotropic distributions are shown in the next section. At this point, it is interesting to analyze what happens when the ratio ρ is finite. Figure 5 shows the same initial distribution as Fig. 4 except that the ratio $\rho=1$ at the maximum of the distribution. The projected image [Fig. 5(b)] is then completely distorted as compared to Fig. 4(b). One can see in particular a broad peak at the center of the image, corresponding to electrons emitted towards the detector, and a larger ring outside corresponding to electrons emitted in the opposite direction. We will see below what kind of error is introduced when inverting such images with the simple back-projection method described below.

B. Inversion method

As quoted previously, different inversion methods may be used in order to extract the physical information from the experimental images resulting from the projection: Abel inversion, onion-peeling methods, etc. (see, for example, Ref. 19). However, owing to the specific expression of the projection operator $\mathscr{T}$, it is more convenient, and more accurate, to invert directly Eqs. (19′) and (21) than using approximate numerical methods like the Abel inversion. In the limit of large ρ values, the projection is a one-dimensional process. The summation in Eq. (21) over the index i may be done in any order (ascending or descending) but the inversion itself must be done from the outer regions of the image to the inner regions, i.e., in descending order with respect to i. This is due to the fact that, at a given radius R_1 on the detector, all electrons with an initial kinetic energy larger than a threshold $W_1=\alpha R_1^2$ contribute to the image. The scheme of the deconvolution process is the following: starting from the outer edge of the image at pixel $(i_0=N, j_0)$ (where N is the largest i value), we assign any signal to electrons emitted with an initial angle $\Phi=0°$ and thus an energy $W_1=\alpha R_1^2$. From the number of electrons found at a given pixel (i_0,j_0), one can then deduce the total number of electrons ejected at any

angle Φ with that given energy. This allows us to calculate the contribution of electrons at this energy to the signal at pixel $i=1...i_0$ according to the definition of the projection operator $\mathscr{F}$. This electron signal is then added to the back-projected image at the pixel position (i_0,j_0), and subtracted from the projected (experimental) image at all pixel position (i,j_0) (with $i \leqslant i_0$). This procedure is repeated for the next lower value (i_0-1) until the center of the image is reached. The whole procedure is done for each line (different j values) separately. The mathematical expression of the inversion algorithm is as follows. For all j values; for $i=N$ down to 1:

for all $i_0 \leqslant i$:

$$F_{XZ}^{(i)}(i_0,j)=F_{XZ}^{(i+1)}(i_0,j)-\frac{\mathscr{F}(i,i_0,j)}{\mathscr{F}(i,i,j)}F_{XZ}^{(i+1)}(i,j),$$

$$F_{R\Theta}^{(i)}(i,j)=F_{R\Theta}^{(i+1)}(i,j)+\frac{F_{XZ}^{(i+1)}(i,j)}{\sin(\theta_0)}, \tag{22}$$

where the angle Θ_0 is defined by relation (20), and $F_{XZ}^{(N+1)}$ is the original projected (or experimental) image before inversion. In the energy-angle coordinates, we start with $F_{R\Theta}^{(N+1)} \equiv 0$. After the N loops of the procedure (from $i=N$ down to $i=1$), one finds the final inverted image $F_{R\Theta}^{(1)}$ and the residual image must be $F_{XZ}^{(1)} \equiv 0$.

Since this back-projection method is exactly the inverse of the projection method described above, it is obvious that simulated projected images will be exactly inverted by Eq. (22), apart from numerical rounding errors. This is clearly visible in Fig. 6, where the initial photoelectron distribution is the sum of three Gaussian distributions corresponding to Y_{00}^2, Y_{10}^2, and Y_{20}^2 (top image). The projected pattern (middle) is a complex superposition of elementary patterns, but the back projection (bottom) returns the original image, and the difference between original and back-projected simulated images is only limited by the precision of the computer. However, the exactness of the back-projection method is somewhat artificial, since both projection and inversion procedures are discrete. If one would use a continuous electron distribution and projection procedure, the necessarily discrete character of the inversion would introduce some minor discrepancies between original and final electron distributions. Such discrepancies would be observed with ''ideal'' experimental projections. However, these discrepancies are inherent to the discrete nature of the data rather than to the approximations made in the calculation of the back projection, which is essentially determined by the expression of the projection operator $\mathscr{F}$.

Let us now analyze what happens when Eq. (22) is used to invert data corresponding to finite values of the energy ratio ρ. According to Eq. (7), the relative energy corresponding to a given radius $R=\sqrt{X^2+Z^2}$ on the image is $\rho=\rho_0/R^2$, where the constant ρ_0 corresponding to $R=1$ is determined by the experimental conditions. Figure 7 presents a typical example of an intermediate ρ value corresponding to standard experimental situation. The original photoelectron distribution [Fig. 7(a)] is the sum of two isotropic distributions centered, respectively, at $R=150$ and 50 pixel units. Choosing $\rho_0=2\times10^6$ in the projection procedure is equivalent to assigning the values $\rho=89$ and 800, respectively, to these energy channels. After projection, we obtain the image in Fig. 7(b). The result of the back projection is presented in Fig. 7(c) and the difference between the original distribution and the back projection in Fig. 7(d). The differences between original and inverted data are small and are visible only in Fig. 7(d). Note that the radius of the outer ring in Fig. 7(d) is

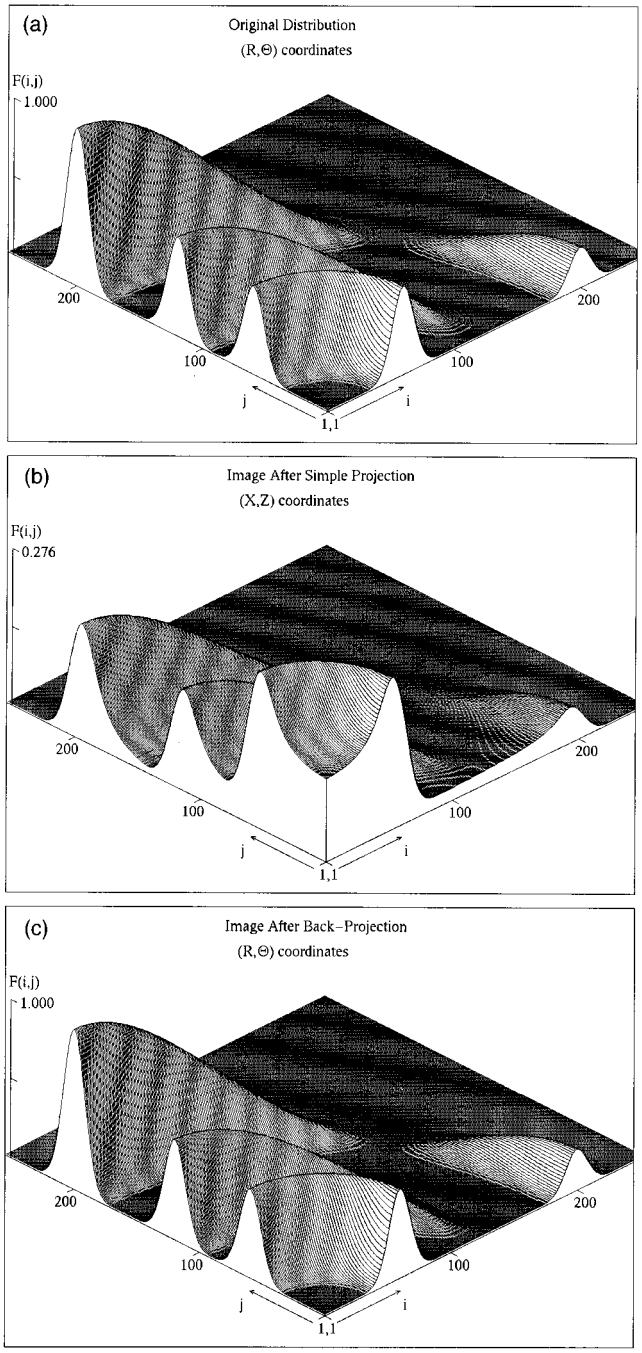

FIG. 6. The initial photoelectron distribution (a) in the frame (R,Θ) is the sum of three Gaussian distributions corresponding to Y_{00}^2, Y_{10}^2, and Y_{20}^2 (top image) with a maximum at $R_0=60$, 120, and 200 pixels, respectively. The projected pattern (b) is a complex superposition of elementary patterns, but the back projection (c) gives exactly the original image and the difference between original and back-projected simulated images is only limited by the precision of the computer.

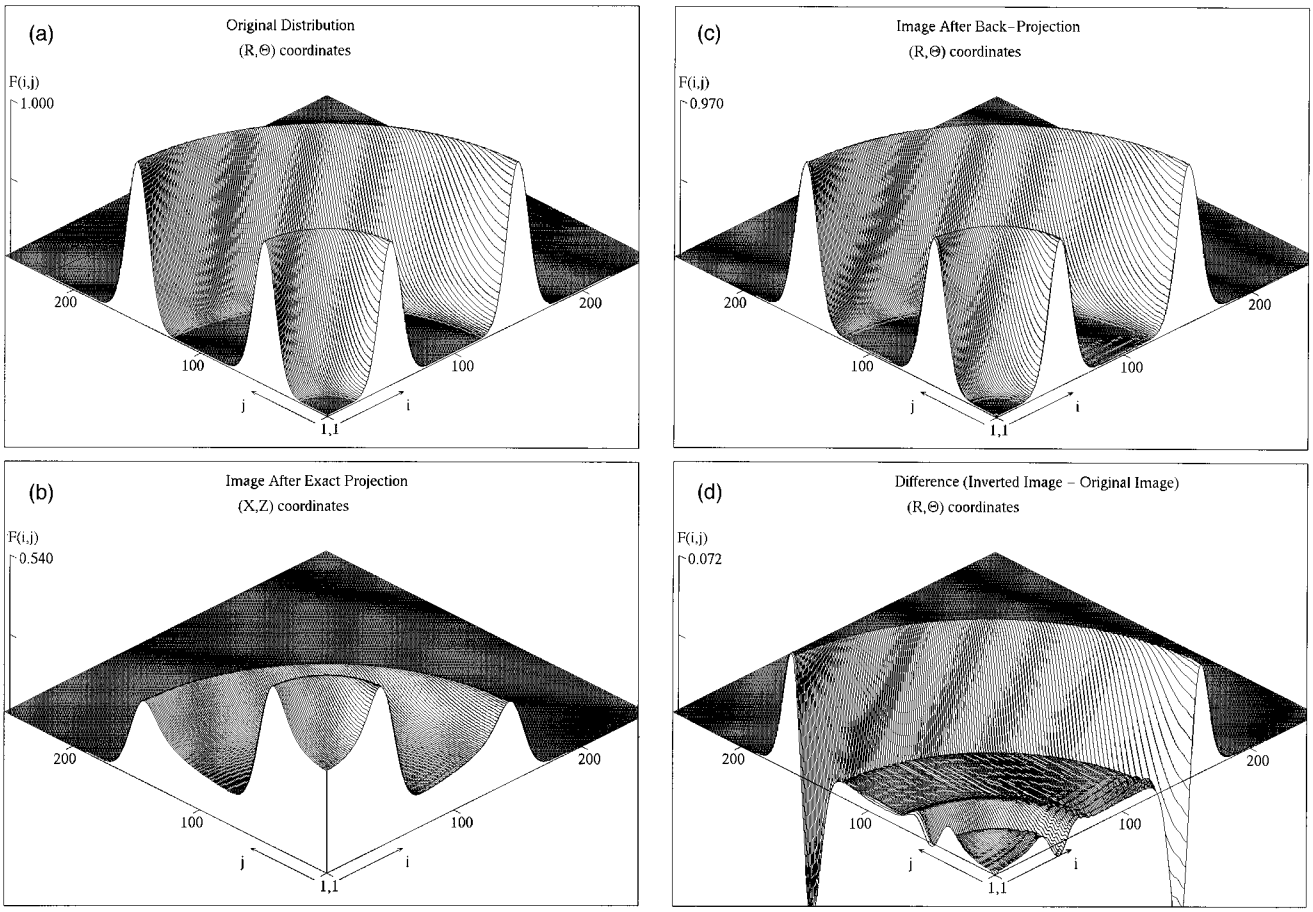

FIG. 7. Typical example of intermediate ρ values corresponding to a standard experimental situation. The original photoelectron distribution (a) is the sum of two isotropic distributions (Y_{00}^2) centered, respectively, at $R=150$ and 50 in pixel units. The projection is made for $\rho_0=2\times10^6$, which is equivalent to assign the values $\rho=89$ and 800, respectively, to the energy channels. After projection, we obtain the image in (b). The result of the back projection is presented in (c) and the difference between the original distribution and the back projection in (d). The difference between original and inverted data is small and is visible only on (d). On the high energy channel, the error amounts to about 7% in intensity, but this corresponds, in fact, to less than 1% error in energy, while the error made for the low energy channel is negligible.

about 0.5% larger than the original diameter, while for the inner ring, this difference is negligible. This is obvious in Fig. 7(d), where the errors made for the outer ring ($\rho\approx100$) are clearly larger than those corresponding to the inner ring ($\rho\sim1000$). The net effect of the finite ρ value in that range of relatively large values is mainly to introduce a small nonlinearity in the energy scale, which increases as ρ decreases, (i.e., as one goes farther from the center of the image). From Eq. (7), it appears that $\rho=100$ corresponds to the condition $(2L/R_{\max})=10$, which is the worst condition that prevails in our experimental setup on the outer edge of the detector. In fact, the distortion of the image due to the small inhomogeneities of the electric field are probably larger, especially on the external zone of the detector where a perfect homogeneity is harder to achieve. As a consequence, we can estimate that, under our specific experimental conditions, the inversion algorithm described by Eqs. (19') and (22) is sufficient.

Let us now investigate smaller ρ values, where the situation becomes more critical. Under the conditions presented in Fig. 5 ($\rho=1$), the back-projection procedure leads to the image of Fig. 8, which is to be compared with Fig. 5(a). The difference between the initial distribution [Fig. 5(a)] and the back-projected image (Fig. 8) is drastic. Under these extreme conditions, the energy scale is not simply distorted, but the apparent energy distribution is wrong: instead of peaking around $R=150$, two lobes appear. Note that for an initially anisotropic distribution, the angular pattern obtained from the inversion procedure would also be distorted. In this case, it is obvious that a more sophisticated inversion procedure is required. This situation arises when the distance between the electron source and the screen is on the same order of magnitude as the image dimension on the detector.

C. Experimental images

As an illustration, we will show two examples of experimental results obtained with the photoelectron imaging spectrometer in four-photon ionization of xenon and molecular hydrogen. Before carrying out the back projection, the center of the experimental image must be determined. Generally, we use a numerical routine that finds the maximum of the function:

$$S=\sum_p T(x_p,y_p)T^*(x_p,y_p)$$

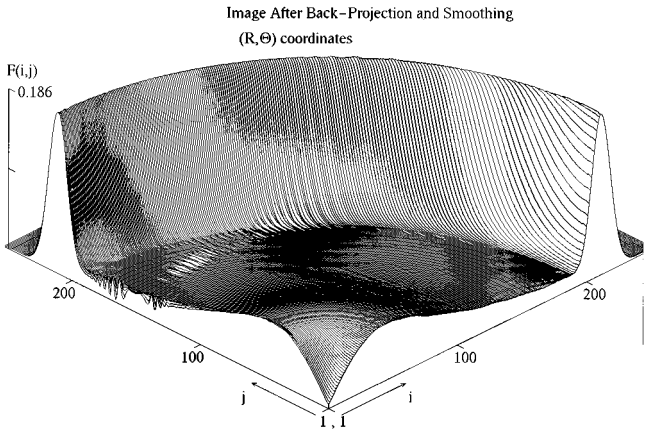

FIG. 8. Back projection in the approximation $\rho \rightarrow \infty$ of the image of Fig. 5(b) obtained by projecting the distribution of Fig. 5(a) with $\rho=1$; compare with Fig. 5(a). The difference between the initial distribution [Fig. 5(a)] and the back-projected image shown here is enormous. Under these extreme conditions, the energy scale is distorted, and the energy distribution is completely wrong; instead of peaking around $R=150$, it presents two lobes, inside and outside.

$$= \sum_p T(x_p, y_p) T(2x_0 - x_p, 2y_0 - y_p), \tag{23}$$

where T refers to the intensity of the original image at the pixel position specified by p, and T^* refers to that of an image obtained by mirroring the original at the trial center position (x_0, y_0). Upon finding the center, the four quadrants of the image are added for better statistical representation and are subjected to the back-projection procedure. As a consequence, the inverted images are symmetric about the vertical (laser polarization) and horizontal axes. Similarly to simulated images, only one fourth of the image is represented in the figures.

There has been recently considerable interest in the study of multiphoton ionization of heavy rare gases in the moderate field regime[20,21] as well as in the strong field regime.[18,22] Rare gas atoms are ideal systems to study multiphoton ionization processes due to the relative simplicity of their electronic structure and to the high value of their ionization potential. However, the detailed interpretation of the observed effects, especially when strong laser fields are used, is often precluded by the complexity of the elementary processes involved. This point has motivated the study described in Ref. 23 concerned with the final state distribution and the respective angular distribution of photoelectrons of about 30 resonant intermediate Rydberg states that participate in four-photon ionization of xenon. The main result of this work is the following: for nd Rydberg states, the branching between the two ionization channel [ground channel: $Xe^+(^2P_{3/2})+e^-$, and excited channel $Xe^+(^2P_{1/2})+e^-$] mirrors the mixing of core states in the three-photon intermediate, while a major deviation from this rule appears for the $ns[\frac{3}{2}](J=1)$ states. The experiments are carried out a near-threshold intensities (1–5 GW/cm^2) using a nanosecond dye laser, linearly polarized, tuned to selectively excite with three-photon transitions the $J=1$ and $J=3$ Rydberg states of xenon lying below the first ionization limit, the absorption of

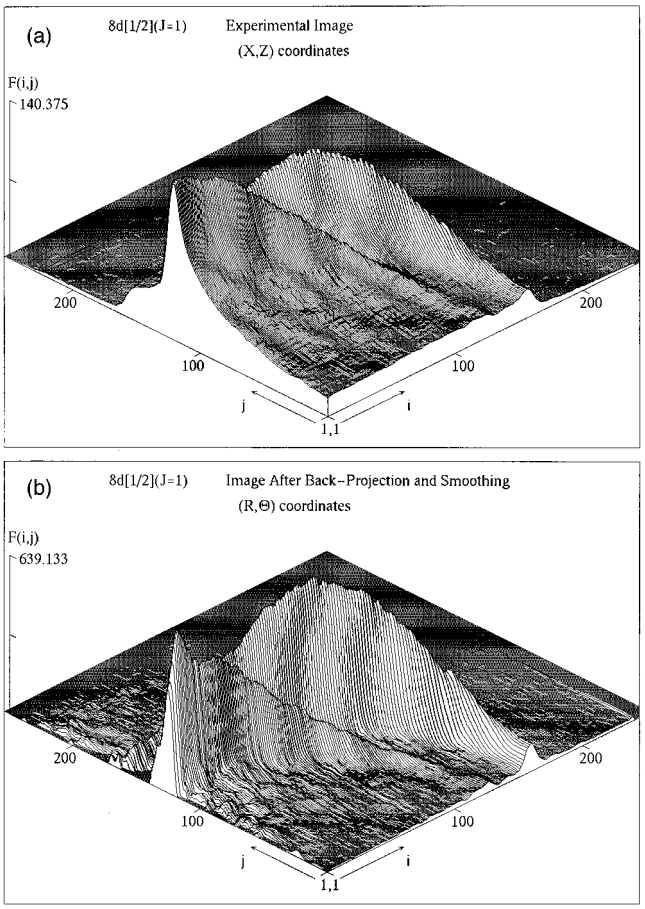

FIG. 9. Example of raw experimental data obtained in resonant four-photon ionization of xenon with the $8d[\frac{1}{2}](J=1)$ intermediate state ($\lambda=318.375$ nm) (a). The corresponding inverted image is presented in (b).

the fourth photon being sufficient to bring the system in the continuum above the first excited states of Xe^+. The photoelectron imaging spectrometer was used to measure the relative ionization yield as well as the angular distribution in both ionization channels: $[Xe^+(^2P_{3/2})+e^-]$ and excited $[Xe^+(^2P_{1/2})+e^-]$. An example of a raw experimental data recorded with the $8d[\frac{1}{2}](J=1)$ intermediate state ($\lambda=318.375$ nm) is shown in Fig. 9(a). The corresponding inverted image is presented in Fig. 9(b). The analysis of this image provides the photoelectron energy spectrum [Fig. 10(a)] and the angular distribution in both channels [Fig. 10(b)]. The advantage of using the imaging spectrometer in this experiment is that it allows a fast and direct view of the processes involved in the four-photon ionization with a good reliability as far as branching ratios and angular distributions are concerned. This work is described in more detail in Refs. 23 and 24.

The experiments carried out on xenon do not require high resolution, since the two ionization channels involved in these experiments are separated by about 1.3 eV. The experiments conducted on molecular hydrogen briefly described below are more characteristic of the capabilities of the imaging spectrometer from the point of view of energy resolution.

As a second example, we show a result obtained in the study of three-photon resonance enhanced, four-photon ionization of H_2 with a selected intermediate level of the $B^1\Sigma_u^+$

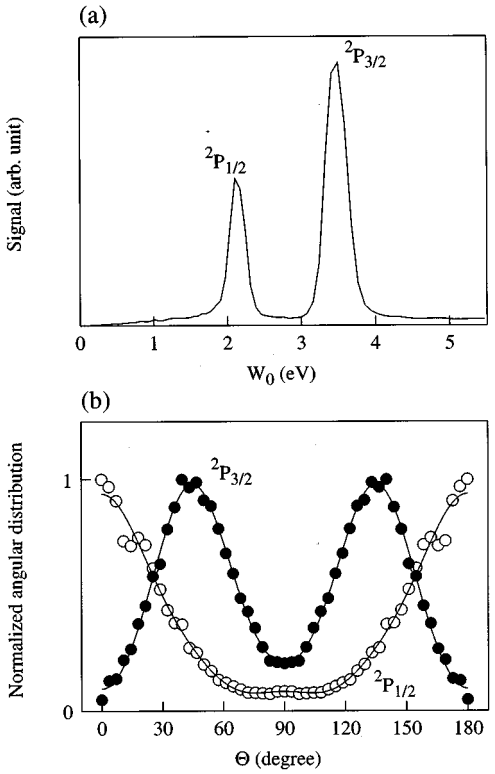

FIG. 10. The analysis of the experimental image presented in Fig. 9 provides the photoelectron energy spectrum (a) and the angular distribution in both ionization channels (b).

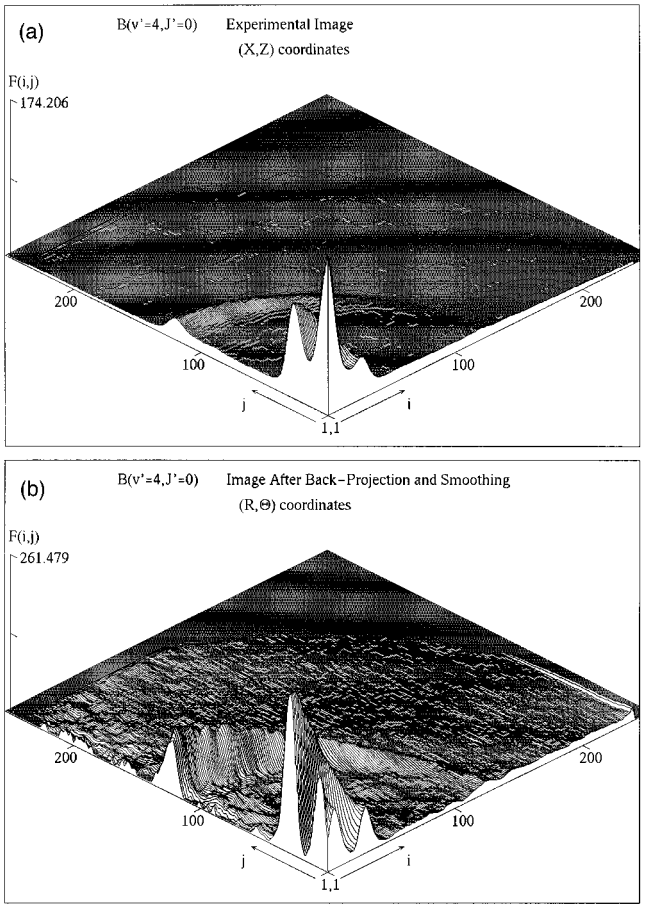

FIG. 11. Typical experimental result obtained in resonant four-photon ionization of H_2 when exciting the $B^1\Sigma_u^+$ ($v'=4$, $J'=0$) intermediate state via the three-photon $P1$ transition: (a) experimental image; (b): inverted image.

state using a tunable UV laser of 5 ns duration, with focal intensities in the range 1–5 GW/cm^2. This kind of transition has been studied by several authors in the past.[25–27] This work, presented in Ref. 28, was mainly concerned with the formation of very low energy photoelectrons and their associated angular distribution. Figure 11 shows a typical experimental result obtained when exciting the $B^1\Sigma_u^+$ ($v'=4$, $J'=0$) intermediate state via the three-photon $P1$ transition. Two competing processes appear:

(1) direct photoionization:

$$H_2 \xrightarrow{+3h\nu} H_2(B^1\Sigma_u^+, v'=4, J'=0)$$
$$\xrightarrow{+h\nu} H_2^+(v^+=0 \text{ or } 1,\ N^+=1 \text{ or } 3)+e^-;$$

(2) photodissociation followed by one-photon ionization of the excited atom:

$$H_2 \xrightarrow{+3h\nu} H_2(B^1\Sigma_u^+, v'=4, J'=0)$$
$$\xrightarrow{+h\nu} H(1s)+H(n=2,l);$$

then, a fifth photon ionizes the excited atom:

$$H(n=2,l) \xrightarrow{+h\nu} H^+ + e^-.$$

Five ionization channels are open at 2 and 39 meV for $v^+=1$ (respectively, $N^+=3$ and 1), 274 and 310 meV for $v^+=0$ (respectively, $N^+=3$ and 1), and 533 meV for the dissociative channel.

Note (see Fig. 12) that the slow electron peaks at 2 and 39 meV are fully resolved, while the two rotational branches of the ground vibrational channel are not distinguishable. This is a result of the fact that the absolute velocity resolution is a constant over the whole spectrum. As a consequence; the energy resolution drastically decreases as the en-

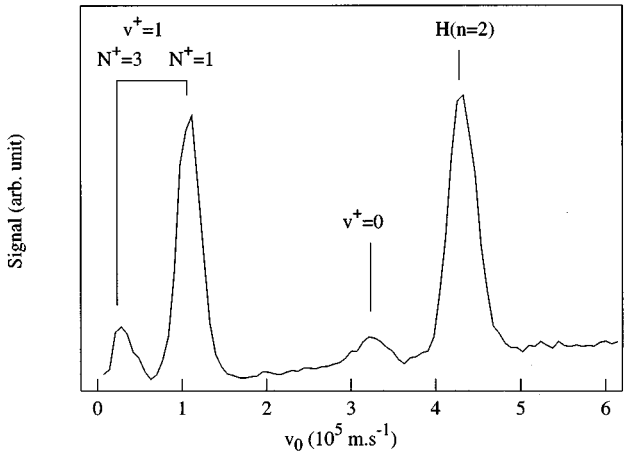

FIG. 12. Energy spectrum derived from the image of Fig. 11. Five ionization channels are open at 2 and 39 meV for $v^+=1$ (respectively, $N^+=3$ and 1), 274 meV, and 310 meV for $v^+=0$ (respectively, $N^+=3$ and 1), and 533 meV for the dissociative channel. Note that the slow electron peaks at 2 and 39 meV are fully resolved, while the two rotational branches of the ground vibrational channel are not distinguishable. This result clearly shows that the energy resolution drastically decreases as the energy increases.

ergy increases. As compared to previous results,[25–27] there is a sensible improvement of the resolution at low energy, while the resolution is lower above 0.5 eV. The point of interest for the present discussion is that, at threshold, a resolution on the order of 1 meV is easily achievable, while, at higher energy, conventional spectrometers are probably better from the point of view of the energy resolution. Further improvements of this kind of spectrometer will probably allow this system to become competitive, in terms of resolution, with ZEKE-PES[15–17] at threshold, with a much larger flexibility in the use of the apparatus.

IV. PROSPECTS

In this article, we have presented the experimental principle of the photoelectron imaging spectrometer, together with the simplest inversion method that allows one to extract significant physical information from the experimental data. The direct back-projection method has been preferred to the common Abel inversion method owing to the specific nature of the photoelectron projection process. Note, however, that this method works properly only in the limit of large ρ (electrostatic energy to initial kinetic energy ratio) values and gives qualitatively the same results as a standard inversion method, although it is more easily extended to the domain of low ρ values.

The photoelectron imaging is being currently improved following two complementary directions. First, the spectrometer itself would have better performance with a larger detector. Indeed, the velocity resolution is mainly limited by the ratio between the effective diameter of the photoelectron detector and the electron source size. In most cases, the size of the region where photoelectrons are formed cannot be reduced arbitrarily and is governed by experimental conditions: density of species of interest, dimensions of a ion or laser beam, etc. It is thus of primary interest to increase the size of the detector. However, the extremely high efficiency of the modern CCD cooled camera allows one to work with very low gain electron to photon converters. Thus, a simple phosphorescent screen coupled to a postacceleration of the photoelectrons may be sufficient when using a high performance CCD camera. Under these conditions, detectors larger than 100 mm may be realized, allowing one to optimize the use of a high-resolution (512×512 pixels or better) camera, which exceeds in performance, in the current experiment, the resolution of the MCP-phosphor screen itself. Along with this technological modification, a second improvement is in progress. As noted previously, the back-projection method described here is relevant only when one is concerned with large ρ values. The full two-dimensional transformation relevant to any range of energy based on the set of exact Eqs. (3) will be presented in a forthcoming article.

Finally, it must be emphasized that bidimensional detectors combining electron or ion to photon conversion coupled to CCD systems may be used in a wide variety of experiments such as photoionization and photodetachment, but also photodissociation and photofragmentation of complex species. For example, in the ''Laboratoire de Spectrométrie Ionique et Moléculaire,'' such a system is currently being coupled to the ion time-of-flight mass spectrometer of a laser vaporization cluster source in order to study the photodetachment of negative metallic cluster ions.

ACKNOWLEDGMENT

The ''Laboratoire de Spectrométrie Ionique et Moléculaire'' is a ''Unité Mixte de Recherche du CNRS, Grant No. 5579''.

[1] J. Berkowitz, *Photoabsorption, Photoionization, and Photoelectron Spectroscopy* (Academic, New York, 1979).
[2] S. Edelstein, M. Lambropoulos, J. A. Duncanson, and R. S. Berry, Phys. Rev. A **9**, 2459 (1974).
[3] R. N. Compton, J. C. Miller, A. E. Carter, and P. Kruit, Chem. Phys. Lett. **71**, 87 (1980).
[4] P. Kruit, J. Kimman, H. G. Müller, and M. J. Van der Wiel, J. Phys. B **16**, 937 (1983).
[5] E. Matthias, P. Zoller, D. S. Elliott, N. D. Piltch, S. J. Smith, and G. Leuchs, Phys. Rev. Lett. **50**, 1914 (1983).
[6] W. A. De Heer, Rev. Mod. Phys. **65**, 611 (1993).
[7] K. Rademann, Ber. Bunseges. Phys. Chem. **95**, 563 (1989).
[8] K. H. Meiwes-Broer, in *Advances in Metal and Semiconductor Clusters*, edited by M. Duncan (JAI, Greenwich, 1993), Vol. 1, p. 37.
[9] M. G. White, W. A. Chupka, M. Seaver, A. Woodward, and S. D. Colson, J. Chem. Phys. **80**, 678 (1984).
[10] Y. Achiba, K. Sato, and K. Kimura, J. Chem. Phys. **82** 3959 (1985).
[11] S. T. Pratt, P. M. Dehmer, and J. L. Dehmer, J. Chem. Phys. **85**, 3379 (1986).
[12] P. J. Miller, W. A. Chupka, J. Winniczek, and M. G. White, J. Chem. Phys. **89**, 4058 (1988).
[13] S. W. Allendorf, D. J. Leahy, D. C. Jacobs, and R. N. Zare, J. Chem. Phys. **91**, 2216 (1989).
[14] P. Kruit and F. H. Read, J. Phys. E **16**, 313 (1983).
[15] M. Sander, L. A. Chewter, K. Müller-Dethlefs, and E. W. Schlag, Phys. Rev. A **36**, 4543 (1987).
[16] L. A. Chewter, M. Sander, K. Müller-Dethlefs, and E. W. Schlag, J. Chem. Phys. **86**, 4737 (1987).
[17] K. Müller-Dethlefs and E. W. Schlag, Annu. Rev. Phys. Chem. **42**, 109 (1991).
[18] H. Helm, N. Bjerre, M. J. Dyer, D. L. Huestis, and M. Saeed, Phys. Rev. Lett. **70**, 3221 (1993).
[19] C. J. Dash, Appl. Opt. **31**, 1146 (1992).
[20] S. T. Pratt, P. M. Dehmer, and J. L. Dehmer, Phys. Rev. A **35**, 3793 (1987).
[21] K. Sato, Y. Achiba, and K. Kimura, J. Chem. Phys. **80**, 57 (1984).
[22] M. D. Perry and O. L. Landen, Phys. Rev. A **38**, 2815 (1988).
[23] C. Bordas, M. J. Dyer, T. A. Fairfield, H. Helm, and K. C. Kulander, Phys. Rev. A **51**, 3726 (1995).
[24] C. Bordas, M. J. Dyer, T. A. Fairfield, M. Saeed, and H. Helm, J. Phys. (Paris) IV **C4**, 647 (1994).
[25] S. T. Pratt, P. M. Dehmer, and J. L. Dehmer, J. Chem. Phys. **78**, 4315 (1983); Chem. Phys. Lett. **105**, 28 (1984).
[26] J. H. M. Bonnie, J. W. Verschuur, H. J. Hopman, and H. B. van Linden van den Heuvell, Chem. Phys. Lett. **130**, 43 (1986).
[27] E. Y. Xu, T. Tsuboi, R. Kachru, and H. Helm, Phys. Rev. A **36**, 5645 (1987).
[28] C. Bordas, M. J. Dyer, and H. Helm, J. Phys. (Paris) IV **C4**, 691 (1994).